

Thermal optimization of second harmonic generation at high pump powers

Alexander Sahn,* Mirko Uebernickel, Katrin Paschke, Götz Erbert, and Günther Tränkle

Ferdinand-Braun-Institut, Leibniz-Institut für Höchstfrequenztechnik, Gustav-Kirchhoff-Str. 4, 12489 Berlin, Germany

*Alexander.Sahn@FBH-Berlin.de

Abstract: We measure the temperature distribution of a 3 cm long periodically poled LiNbO₃ crystal in a single-pass second harmonic generation (SHG) setup at 488 nm. By means of three resistance heaters and directly mounted Pt100 sensors the crystal is subdivided in three sections. 9.4 W infrared pump light and 1.3 W of SHG light cause a de-homogenized temperature distribution of 0.2 K between the middle and back section. A sectional offset heating is used to homogenize the temperature in those two sections and thus increasing the conversion efficiency. A 15% higher SHG output power matching the prediction of our theoretical model is achieved.

©2011 Optical Society of America

OCIS codes: (140.2020) Diode lasers; (140.3515) Lasers, frequency doubled; (190.2620) Harmonic generation and mixing; (140.6810) Thermal effects.

References and links

1. M. Maiwald, D. Jedrzejczyk, A. Sahn, K. Paschke, R. Güther, B. Sumpf, G. Erbert, and G. Tränkle, "Second-harmonic-generation microsystem light source at 488 nm for Raman spectroscopy," *Opt. Lett.* **34**(2), 217–219 (2009).
2. W. Schulz and R. Poprawe, "Manufacturing with novel high-power diode lasers," *IEEE J. Sel. Top. Quantum Electron.* **6**(4), 696–705 (2000).
3. G. Hollemann, B. Braun, P. Heist, J. Symanowski, U. Krause, J. Kraenert, and C. Deter, "High-power laser projection displays," *Proc. SPIE* **4294**, 36–46 (2001).
4. M. Maiwald, S. Schwertfeger, R. Güther, B. Sumpf, K. Paschke, C. Dzionk, G. Erbert, and G. Tränkle, "600 mW optical output power at 488 nm by use of a high-power hybrid laser diode system and a periodically poled MgO:LiNbO₃ bulk crystal," *Opt. Lett.* **31**(6), 802–804 (2006).
5. O. B. Jensen, P. E. Andersen, B. Sumpf, K. H. Hasler, G. Erbert, and P. M. Petersen, "1.5 W green light generation by single-pass second harmonic generation of a single-frequency tapered diode laser," *Opt. Express* **17**(8), 6532–6539 (2009).
6. C. Fiebig, A. Sahn, M. Uebernickel, G. Blume, B. Eppich, K. Paschke, and G. Erbert, "Compact second-harmonic generation laser module with 1 W optical output power at 490 nm," *Opt. Express* **17**(25), 22785–22790 (2009).
7. P. Q. Liu, C. Fiebig, M. Uebernickel, G. Blume, D. Feise, A. Sahn, D. Jedrzejczyk, K. Paschke, and G. Erbert, "High-power (1.1 W) green (532 nm) laser source based on single-pass second harmonic generation on a compact micro-optical bench," *Proc. SPIE* **7917**, 791704, 791704-7 (2011).
8. M. Uebernickel, R. Güther, G. Blume, C. Fiebig, K. Paschke, and G. Erbert, "Study of the properties of the SHG with diode lasers," *Appl. Phys. B* **99**(3), 457–464 (2010).
9. C. Fiebig, G. Blume, M. Uebernickel, D. Feise, C. Kaspari, K. Paschke, J. Fricke, H. Wenzel, and G. Erbert, "High-power DBR tapered laser at 980 nm for single path second harmonic generation," *IEEE J. Sel. Top. Quantum Electron.* **15**(3), 978–983 (2009).
10. Y. L. Lee, Y. Noh, C. Jung, T. J. Yu, B. Yu, J. Lee, D. Ko, and K. Oh, "Reshaping of a second-harmonic curve in periodically poled Ti:LiNbO₃ channel waveguide by a local-temperature-control technique," *Appl. Phys. Lett.* **86**(1), 011104 (2005).
11. G. D. Boyd and D. A. Kleinman, "Parametric interaction of focused Gaussian light beams," *J. Appl. Phys.* **39**(8), 3597–3639 (1968).
12. D. Jedrzejczyk, R. Güther, K. Paschke, B. Eppich, and G. Erbert, "200 mW at 488 nm from a ppMgO:LN ridge waveguide by frequency doubling of a laser diode module," *IEEE Photon. Technol. Lett.* **22**(17), 1282–1284 (2010).
13. O. Louchev, N. Yu, S. Kurimura, and K. Kitamura, "Nanosecond pulsed laser energy and thermal field evolution during second harmonic generation in periodically poled LiNbO₃ crystals," *J. Appl. Phys.* **98**(11), 113103 (2005).
14. O. Gayer, Z. Sacks, E. Galun, and A. Arie, "Temperature and wavelength dependent refractive index equations for MgO-doped congruent and stoichiometric LiNbO₃," *Appl. Phys. B* **91**(2), 343–348 (2008).

1. Introduction

High power lasers emitting in the visible spectral range are required in many fields, such as spectroscopy [1], direct material processing [2] and display technology [3]. Gas and solid state lasers are readily available for these purposes but they are limited to specific wavelengths and their size can prevent their use in some applications.

Laser diodes can overcome these limitations. The frequency conversion—especially the Second Harmonic Generation (SHG)—is a feasible way to create visible light from NIR diode laser sources. Previous works have shown the advantages of the single-pass SHG for high output powers [4,5]. Such setups can be miniaturized to laser modules with less than $2,5 \text{ cm}^3$ [6,7]. Those modules are small, efficient and can be customized to many wavelengths by a periodical poling of the used nonlinear crystal. This method is called quasi phase-matching (QPM) and is applicable for the whole transparency range of the material.

Periodically poled MgO doped LiNbO_3 (PPLN) crystals were used in the aforementioned works. PPLN features a high nonlinear coefficient, which results in a high conversion efficiency. The conversion efficiency is a function of different parameters such as the spectral width, power and beam quality of the pump source. While Gaussian beams have the best conversion efficiency due to the highest possible beam quality, laser diodes with non-diffraction limited beams can also be used for the frequency conversion [8]. With a narrow spectral width, a good spectral stability, a high output power, and a good beam quality distributed Bragg reflector tapered lasers (DBR-TPL) are well-suited for frequency conversion [9].

We achieve frequency conversion by heating the crystal whereby the accepted wavelength bandwidth can be shifted by approximately $100 \text{ pm} / \text{K}$ at 976 nm at around 50° C . The temperature distribution at the light path in the crystal has to be homogeneous [10,11]. Any discrepancy diminishes the effective crystal length (the length of the phase matched poling period) and thereby the conversion efficiency.

At high pump powers the conversion efficiency drops below expectations [12]. Previous works suggest an absorption of the SH power in the crystal, and thereby an inhomogeneous temperature distribution that leads to a drop in the conversion efficiency [13]. This work will examine the temperature effects at high pump powers for a continuous wave (cw) operation. To counter the inhomogeneous temperature distribution a special crystal package is devised. It allows the setting of arbitrary temperature distributions along the crystal length that in turn maximizes the effective crystal length and thereby the conversion efficiency.

2. Experimental setup

2.1 IR pump source

The IR pump source is a DBR-TPL as described in [9]. It is a 6 mm long laser with a tapered section of 4 mm , a ridge waveguide (RW) section and a DBR section of 1 mm each. With the heat sink temperature set to 10° C the laser provides an optical output power of $P_{\text{out}} = 10.5 \text{ W}$ at a wavelength of $\lambda = 975.2 \text{ nm}$ and a spectral width of $\Delta\lambda_{\text{FWHM}} = 14 \text{ pm}$. During the experiments λ and $\Delta\lambda_{\text{FWHM}}$ were monitored using a Double Echelle Monochromator (DEMON). This way we ensured that no mode hops or changes in the spectral width beyond the measurement resolution occurred. The beam quality was measured beforehand and was found to be $M^2_{\sigma, \text{lat.}} = 14$ and $M^2_{\sigma, \text{vert.}} = 2$, according to ISO 11146 using the method of second order moments. The measurement was done at the position of the crystal after the beam has passed all previous optical elements. The power content of the main lobe is about 60%. The short-term power stability is in the 3% range.

2.2 Optical system

Figure 1 shows the side view of the experimental setup. The emitted beam is collimated in the vertical direction by an aspheric lens ($f = 8 \text{ mm}$). A cylindrical lens ($f = 100 \text{ mm}$) is used to collimate in the lateral direction and to compensate the astigmatism of the DBR-TPL. The

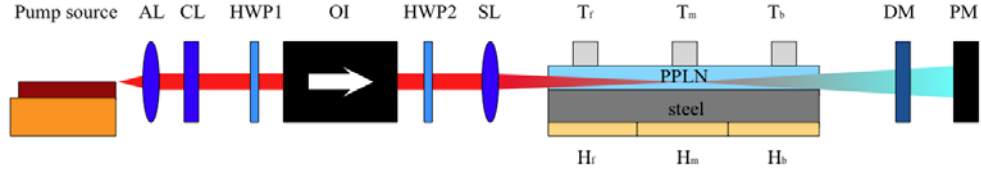


Fig. 1. Experimental setup: AL: aspheric lens, CL: cylindrical lens, HWP: half wave plate, OI: optical isolator, SL: spherical lens, T: temperature sensors, PPLN: PPLN crystal, H: offset heaters, steel: heat spreader and mount, DM dichroic mirror, PM: thermal power meter

collimated beam is then guided through an optical isolator (OI). The OI has a forward transmission of 90% and a backward suppression of more than -40 dB to avoid IR back reflections into the laser. A half-wave-plate (HWP1) in front of the OI allows a scaling of the power with no influence on other beam properties. At the backside of the OI a half-wave-plate (HWP2) is used to match the crystals accepted polarization. With a spherical lens ($f = 175$ mm) the beam is then focused into the PPLN crystal. A dichroic mirror reflects 99.9% of the unconverted IR light after it passes the crystal into a beam dump. The transmission of the visible light is 92%. A thermal power meter (PM) monitors the SHG power. The maximum achievable pump power in front of the crystal was measured to be 9.4 W.

2.3 PPLN crystal and package

The PPLN crystal's dimensions ($h \times w \times l$) are $0.5 \times 2 \times 30 \text{ mm}^3$. It has a MgO doping of 5% and was manufactured by HC Photonics. The periodical poling runs along the whole length of the crystal. For $\lambda = 976 \text{ nm}$ and a poling period of $\Lambda = 5.25 \mu\text{m}$ the QPM temperature is $T_{\text{PM}} = 50^\circ\text{C}$. We simulated the temperature curve as shown in Fig. 2 according to the theory of Boyd and Kleinman [11] using the optimal focusing condition. Equation (1) and Eq. (2) are used to describe the poling period Λ and the dispersion Δn_e :

$$\Lambda(T, \lambda) = \frac{\lambda}{2 \times \Delta n_e(T, \lambda)}, \quad (1)$$

$$\Delta n_e(T, \lambda) = n_e\left(T, \frac{\lambda}{2}\right) - n_e(T, \lambda). \quad (2)$$

The index of refraction was calculated with the Sellmeier equations after [14]. This simulation is only valid for non-depleted Gaussian beams and can be seen as an approximation for the non-diffraction-limited beam of the used diode laser. It shows a 15% lower SHG output power for a temperature deviation of $\pm 0.17 \text{ K}$ from T_{PM} . The full-width-at-half-maximum (FWHM) value for the phase matching temperature is 0.68 K . This is the

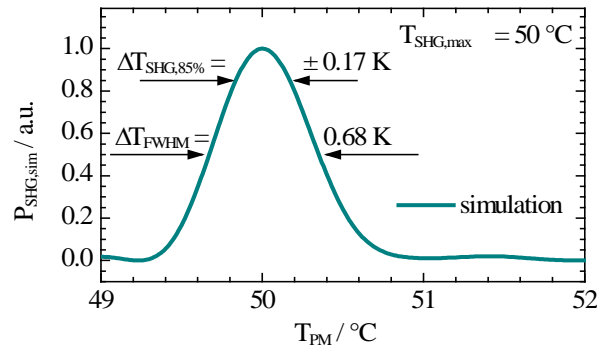


Fig. 2. Simulated SHG phase match temperature curve for our given crystal. The theory is valid for a Gaussian beam. A temperature deviation of $\pm 0.17 \text{ K}$ from the optimal phase match temperature leads to a 15% lower SHG output power.

optimal achievable value for a 3 cm crystal with a homogeneous QPM temperature over its whole length. Reducing the effective crystal length by an inhomogeneous temperature distribution increases ΔT_{FWHM} .

The crystal package is designed specifically for this experiment. It is a modified version of the package used in the aforementioned laser modules. The crystal is bonded onto a stainless steel plate that acts as a heat spreader and mechanical mount. Three resistance micro heaters of 10 mm length are bonded onto the other side of the heat spreader forming three sections. The low thermal conductivity of steel allows a better local heating of the different sections. The micro heaters have a resistance in the 2.3 Ω range and are driven by a constant current source allowing an offset heating of the sections. Corresponding to each of the sections, Pt100 sensors are mounted directly onto the opposite surface of the crystal. The background temperature of the whole package is applied by a close loop controlled heat sink. The thermal expansion coefficients of crystal, steel plate and heaters are well matched to avoid mechanical stresses during mounting and heat cycles.

2.4 Methods for measurements

Using Pt100 temperature sensors, the temperatures of the three sections of the crystal are monitored with a resolution of $\Delta T_{\text{res}} = \pm 0.01$ K. The expected error of measurement of $\Delta T_{\text{err,abs}} = \pm 0.25$ K for absolute temperature values is compensated by calculating the relative temperature change. By subtracting the starting point temperatures for all measure points, we achieve an error of measurement of $\Delta T_{\text{err,rel}} = \pm 0.05$ K.

The dichroic mirror in front of the power meter reflects about 8% of the SHG light. All SHG power values are corrected accordingly.

3. Experimental results

For a better understanding of the thermal processes, two approaches for the measurements were made. A static measurement analyzes the steady state of the system at cw operation at T_{PM} . T_{PM} is around 48°C in the low power regime with the wavelength of the laser at $\lambda = 975.2$ nm. A dynamic measurement involves a temperature sweep of about $T_{\text{PM}} - 1.5$ K $< T_{\text{PM}} < T_{\text{PM}} + 1.5$ K. The sweep is performed with about 0.3 K/min.

3.1 Static case

With only IR light passing through the crystal at a temperature well below T_{PM} we were able to measure a temperature effect due to IR absorption. The absolute temperatures and the relative temperature changes of the three sections are shown in Fig. 3a for different pump powers. The point of reference for the three sections is at $P_{\text{pump}} = 0$ W. The temperature increase in all three sections is proportional to the pump power. The front section has the highest slope, the back section the lowest and the middle section lies in between. This is caused by scattered light hitting the steel heat spreader. Since steel has a poor thermal conductivity the temperature is not well homogenized. An absorption of IR power at the first temperature sensor can be ruled out. The front section's sensor would block the IR light, yet the middle section's sensor registers a temperature increase. $P_{\text{pump}} = 9.4$ W results in $\Delta T_{\text{m}} = 1.1$ K in the middle section and $\Delta T_{\text{b}} = 0.8$ K in the back section leading to a temperature difference $\Delta T_{\text{m-b}} = 0.3$ K.

The second measurement involves the temperatures with SH and IR light being present in the crystal. For each point the QPM temperature had to be adjusted to the point of highest SHG output power using the heat sink. The three section's temperatures are plotted over P_{SHG} with the corresponding pump power noted in the plot (Fig. 3b). With rising P_{SHG} the average absolute temperature shown in the upper part of the plot is decreased. The lower part of the plot shows relative temperature changes with the reference temperatures at $P_{\text{pump}} = 2$ W where no measurable temperature effects due to SH absorption take place (see also Fig. 5a below). For 4 W of pump power, the relative temperature movement is still similar to the case without SH light being present. With increasing SH power the back section is heated up

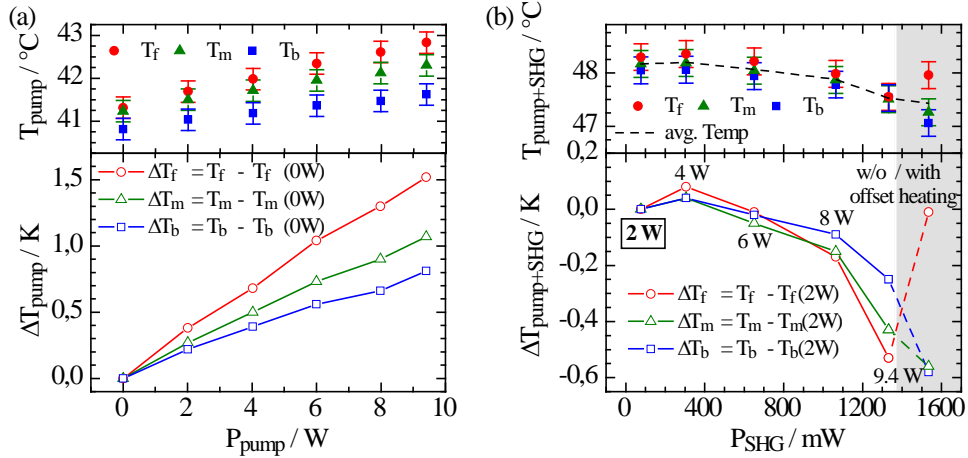


Fig. 3. Upper parts of the plots show the absolute temperature values with an error of measurement of 0.5 K. The lower parts show the relative temperature behavior in respect to a given point of reference. In (a) the temperature behavior due to IR light passing the crystal is shown. In (b) the temperature behavior due to the combination of IR and SH light in the crystal is shown.

disproportionally, causing a smaller relative temperature movement compared to the other sections.

Only after applying an offset heating the distribution can be reversed again (Fig. 3, dashed area). Especially the temperature behavior between the middle (ΔT_m) and the back section (ΔT_b) is here almost the same as it was at low pump powers.

For an offset heating using the front heater, Fig. 4a shows the temperature response of all sections. Carefully adjusting the front section's heating current while reducing the overall heat sink temperature results in higher SH output powers. We mapped P_{SHG} over the temperature difference of middle and back section in the range of $-0.12 \text{ K} < \Delta T_{m-b} < 0.3 \text{ K}$ (Fig. 4b). P_{SHG} peaks at 1550 mW where ΔT_{m-b} is close to 0 K. The corresponding heating current is $I_f = 170 \text{ mA}$ ($P_f = 72 \text{ mW}$) which according to Fig. 4a would result in a temperature difference of $\Delta T_{m-b,\text{heater}} = 0.47 \text{ K}$. The increasing SH power heats up the back section. The additional 210 mW of SH power reduces the temperature difference to only $\Delta T_{m-b,\text{res}} = 0.23 \text{ K}$. Increasing the heating power P_f further has no positive effect on P_{SHG} . Completely turning off the offset

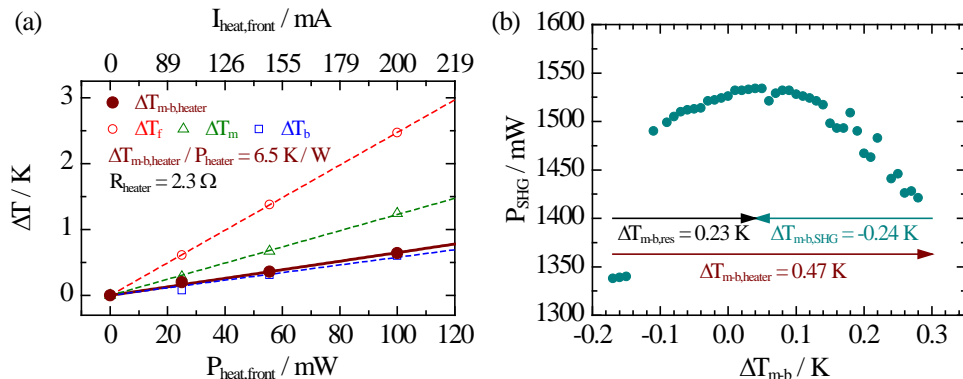


Fig. 4. (a) Measured temperature increase due to heating in the front section. The resulting temperature difference between back and middle section $\Delta T_{m-b,\text{heater}}$ is also shown. (b) Influence of the temperature difference between middle and back section on the SH output power. Arrows indicate the different temperature effects taking place in the crystal simultaneously at the peak power level.

heating, P_{SHG} peaks at 1340 mW with a temperature difference of $\Delta T_{\text{m-b}} = -0.17$ K. These last data points are also shown in the plot to demonstrate the increase of P_{SHG} of 15%.

3.2 Dynamic case

The dynamic case explores the behavior of the system for a temperature sweep with approx. 0.3 K/min. The upper part of the plot shows P_{SHG} over the temperature of the middle section of the crystal. To visualize the SHG temperature effects the influence of the temperature sweep is eliminated and the temperatures are shown in respect to themselves (Fig. 5).

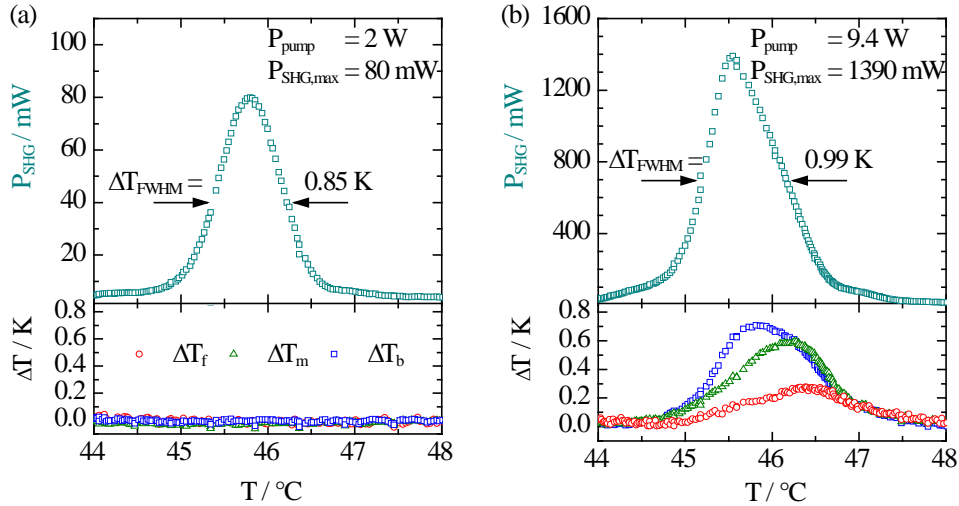


Fig. 5. For a temperature sweep across the phase matching temperature the temperature movement in the three sections is shown. (a) At low pump powers ($P_{\text{pump}} = 2$ W) no relative temperature movement is measurable. (b) At high pump levels ($P_{\text{pump}} = 9.4$ W) a temperature rise in the three sections is evident. The highest rise is in the back section and the lowest in the front. The peaks of the temperature rise for the middle and front section are delayed indicating that most of the heating due to SHG takes place in the back section. The other sections are then heated through the steel heat spreader.

At 2 W pump power the absorption of SH light does not lead to a measurable temperature increase (Fig. 5a, lower plot). The SHG power curve in the upper plot is symmetrical and with $\Delta T_{\text{FWHM}} = 0.85$ K in the same order of magnitude as the simulation. At $P_{\text{pump}} = 9.4$ W the temperature response of the back section is evident (Fig. 5b, lower part). The output power of $P_{\text{SHG}} = 1390$ mW shown in the upper part is higher than in the static case but lower than in the optimized case. A partially deviating QPM temperature reduced the effective crystal length which is indicated by a broader ΔT_{FWHM} of 0.99 K. The delayed temperature peaks of the middle and front section is caused by the low thermal conductivity of the steel heat spreader.

4. Discussion and conclusion

Our measurements show several temperature effects taking place in the crystal during SHG. The IR beam is partially absorbed, heating up the whole crystal. We used the three heaters to emulate the temperature distribution as seen in Fig. 3a. The power to generate this heat is used to estimate the total absorption of the IR light which results to (0.9 ± 0.08) %. The most important effect for this work is the absorption of the generated SH light. With the same technique of estimating the absorbed power we concluded that (5 ± 1) % of the SH light is absorbed in the crystal at SHG output powers above 1 W.

In theory a homogeneous temperature distribution is the precondition for the highest conversion efficiency with a constant duty cycle of the poling period over the whole length of the crystal. If parts of the crystal are not homogeneously heated, the effective crystal length is

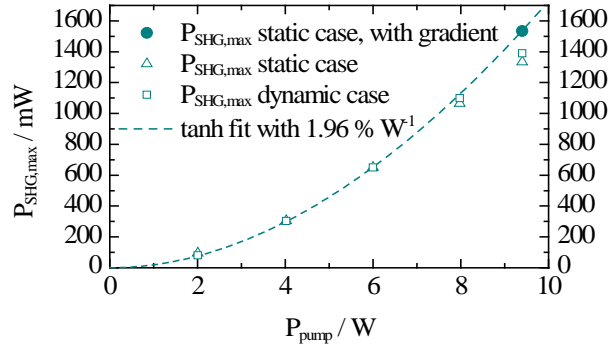


Fig. 6. Peak SHG output powers at different pump power levels. For the first three data points a depletion fit with a conversion efficiency of $1.96\%W^{-1}$ was calculated. At higher pump powers P_{SHG} deviates. Through the application of an offset heating in the front section of the crystal the calculated efficiency is met again.

reduced which results in a lower conversion efficiency. This is due to a dephasing of the fundamental and second harmonic wave, as the dispersion depends on the temperature (Eq. (2)).

The dependence of the second harmonic output power on the pump power is described by a depletion fit. Figure 6 shows this fit for the measurements from 2 W to 6 W pump power with a conversion efficiency of $\eta = 1.96\%W^{-1}$. Here, the peak powers of the static and dynamic measured cases are equal. For higher SH powers (>1 W) there is a drop in the conversion efficiency. This is caused by a dephasing of the fundamental and second harmonic beam [13].

We explain this dephasing as follows: The SH power grows over the length of the crystal. This causes more power being absorbed in the back section of the crystal leading to higher temperature rise compared to the other sections. We measured a temperature difference between the middle and back section of $\Delta T_{m-b} = -0.17$ K for the highest pump power of 9.4 W (Fig. 4b). In the Boyd-Kleinman theory, such a temperature difference would cause a drop of 15% from the maximum obtainable output power (Fig. 2). With the application of the offset heating in the front section, ΔT_{m-b} is reduced to almost 0 K. This eliminates the dephasing and brings back the conversion efficiency to its original value of $1.96\%W^{-1}$. P_{SHG} was increased by 15% from 1340 mW in the thermal unoptimized case to 1550 mW in the thermal optimized case.

The optimized temperature distribution is shown in Fig. 3b in the dashed area. Please note that only ΔT_m and ΔT_b are at the same temperature level whereas ΔT_f is at a 0.6 K higher temperature level. This contradicts the theory of a homogeneous temperature distribution to obtain the highest conversion efficiency. We propose, that the index of refraction also depends on the intensity of the beams. With the high intensity of the SH light, Δn_e changes, leading to a lower QPM temperature at the end of the crystal. Another indication for that is the decreasing average QPM temperature at higher output powers (Fig. 3b, upper part). Further studies on this effect are necessary for a better understanding and a theoretical model.

In conclusion we were able to optimize the SHG conversion efficiency at high pump powers with the application of an offset heating in the front of the crystal. This leads to a temperature distribution in the middle and back section that is similar to that of lower pump powers. Especially for future SHG experiments at even shorter wavelengths the SHG absorption and the resulting temperature effects will be more influential. The principle of an offset heating will find its way into miniaturized laser modules to push the output powers of those even further.

Acknowledgments

We would like to thank the German Federal Ministry of Education and Research (BMBF) for the funding of this work in the initiative “InnoProfile” (Grant No. 03IP613).